ACS Catalysis

Research Article

pubs.acs.org/acscatalysis

Theoretical Investigation of the Isomerization and Disproportionation of *m*-Xylene over Medium-Pore Zeolites with Different Framework Topologies

Youngchul Byun,[†] Donghui Jo,[†] Dong Nam Shin,[‡] and Suk Bong Hong*[,†]

[†]Center for Ordered Nanoporous Materials Synthesis, School of Environmental Science and Engineering and Department of Chemical Engineering, POSTECH, Pohang 790-784, Korea

[‡]Environmental Research Department, Research Institute of Industrial Science and Technology, Pohang 790-784, Korea

Supporting Information

ABSTRACT: The strain energies of three trimethylated diphenylmethane (3mDPM) and six tetramethylated diphenylmethane (4mDPM) isomers serving as the main reaction intermediates of *m*-xylene isomerization and disproportionation over eight medium-pore zeolites with different framework topologies have been determined theoretically in order to elucidate the effects of zeolite pore structure on this aromatic transformation. Although the strain energies of 3mDPM and 4mDPM derivatives in MCM-22, TNU-9, and NU-87, all of which have large 12-ring cavities/channels, are always lower than 40 kJ mol^{-1}, some of them in cavity-free ZSM-5, ZSM-57, and TNU-10 are characterized by the strain energies higher than 40 kJ mol^{-1}. In particular, all the species in ZSM-22 and ZSM-23 with narrower one-dimensional 10-ring channels have the strain energies much higher than 40 kJ mol^{-1}. On the other hand, the energy difference (<30 kJ mol^{-1}) between the (dimethylphenyl)methylium ion and the transition state for formation of the tetramethylated benzenium-type carbenium ions was calculated to be much lower than the energy barrier (183 kJ mol^{-1}) to the hydride transfer from the reactant molecule. The overall results of this study clearly show that transition-state shape selectivity is responsible for the formation of 3mDPM derivatives, as well as of slightly larger 4mDPM ones, in medium-pore zeolites.

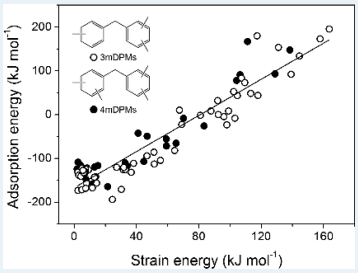

KEYWORDS: *zeolites, m-xylene isomerization and disproportionation, reaction intermediates, DFT calculations, strain energies*

INTRODUCTION

Mechanistic investigations of the transformation of aromatic hydrocarbons over acidic zeolite catalysts are still an active field of research in that the knowledge from such studies is essential not only for the refinement of already known concepts of shape selectivity in heterogeneous catalysis but also for the development of entirely new ones. Conversion of *m*-xylene into its *para*-isomer is of particular importance among the aromatic process technologies because of the great industrial demand of *p*-xylene for manufacturing polyester.[1,2] In fact, remarkable advances in *p*-xylene production from *m*-xylene have been achieved over the last several decades.

The great success of zeolites as catalysts in the isomerization and disproportionation of *m*-xylene is largely due to their unique shape selective properties.[3−15] To clarify the nature of shape selectivity on the product distribution of this aromatic conversion, the reaction mechanisms hidden behind have intensively investigated. Two major types of reaction pathways have been proposed thus far: (i) the monomolecular 1,2-methyl shift mechanism and (ii) the bimolecular mechanism which involves trimethylated diphenylmethane (3mDPM) and tetramethylated diphenylmethane (4mDPM) derivatives as reaction intermediates. Although the existence of both groups of bicyclic organic species has not been experimentally evidenced until a recent date,[15] the latter reaction pathway is much more space-demanding than the former one. Without doubt, therefore, the mechanism of *m*-xylene conversion over medium-pore zeolites has long been considered to be monomolecular.

To gain new insights into the mechanisms of the zeolite-catalyzed isomerization and disproportionation of *m*-xylene, we have recently compared the catalytic properties of a total of 13 medium-pore and 3 large-pore zeolites with different framework topologies for this aromatic transformation and the gas chromatography−mass spectroscopy (GC-MS) results from all used zeolite catalysts.[15] The medium-pore zeolites employed include those containing (i) large 12-ring cavities/channels accessible only through 10-ring windows (H-MCM-22 (framework type MWW), H-TNU-9 (TUN), H-NU-87 (NES), and H-EU-1 (EUO)), (ii) mutually intersection 10-ring channels only (H-ZSM-5 (MFI), H-IM-5 (IMF), and H-ITQ-2), (iii) intersecting 10- and 8-ring channels (H-ZSM-57 (MFS), H-TNU-10 (STI), H-SUZ-4 (SZR), and H-ferrierite (FER)), and (iv) one-dimensional (1D) 10-ring channels only (H-ZSM-22 (TON) and H-ZSM-23(MTT)). Like large-pore zeolites, all members of the first subgroup of medium-pore zeolites were found to allow the formation of both 3mDPM and 4mDPM

Received: February 12, 2014
Revised: April 16, 2014
Published: April 21, 2014

   dx.doi.org/10.1021/cs500186y | ACS Catal. 2014, 4, 1764−1776

derivatives. However, this is not always the case for their other three subgroups.

On the basis of the overall GC-MS results of our recent study, we have proposed a new bimolecular mechanism in which both 3mDPM and 4mDPM derivatives are involved as reaction intermediates in the zeolite-catalyzed *m*-xylene conversion. As shown in Scheme 1, this mechanism starts with hydride

Scheme 1. Bimolecular Reaction Mechanism for the Zeolite-Catalyzed Isomerization and Disproportionation of *m*-Xylene, Where 3mDPM and 4mDPM Are Involved as Reaction Intermediates[a]

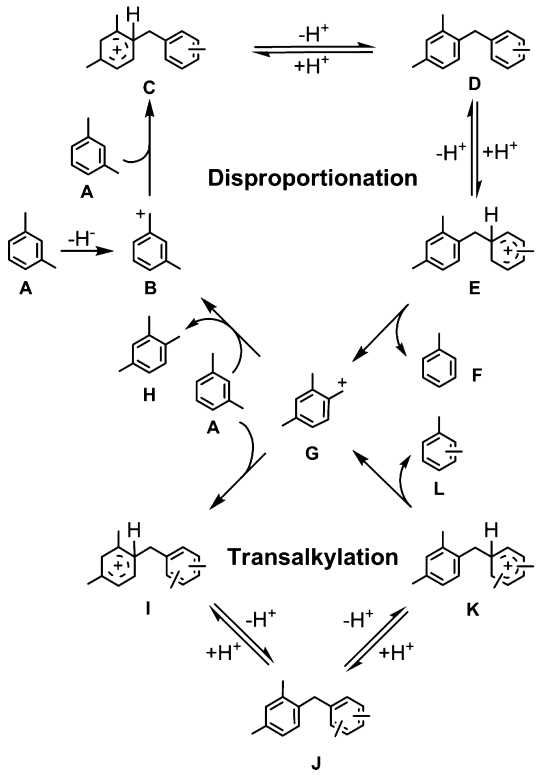

[a]Adapted from ref 15.

abstraction upon adsorption of *m*-xylene molecules (**A**) on the Brønsted acid sites in zeolites to produce the cation (**B**), which can in turn be converted to the alkoxide form of *m*-xylene. Then, species **B** reacts with another *m*-xylene molecule (**A**) to form the trimethylated benzenium-type carbenium ion (**C**) that can be changed to a neutral 3mDPM derivative (**D**) by the proton migration to nearby Brønsted acid sites and again to another benzenium-type carbenium ion (**E**) on nearby but unoccupied Brønsted acid sites. Subsequently, species **E** may split off the (dimethylphenyl)methylium ions **G** and leave a toluene molecule (**F**). Cations **G** further react with another *m*-xylene molecule to produce the tetramethylated benzenium-type carbenium ions (**I** and **K**) and a neutral 4mDPM species (**J**). This is because the hydride abstraction and transfer (**G** to **B**) have the highest energy barrier among the elementary steps in Scheme 1.[15] Therefore, the 3mDPM and 4mDPM species are serving as the reaction intermediates of *m*-xylene disproportionation and transalkylation with **G**, respectively. If such were the case, then the type of reaction intermediates formed would be strongly influenced by the pore shape and size of the zeolite catalyst employed.

Quantum-chemical calculations are a useful means for elucidating the mechanisms of zeolite catalysis, as well as for developing new theories of its shape selectivity.[20−30] Several studies have already concerned the transformation of *m*-xylene. Rozanska et al. have calculated the relative formation energies of reaction intermediates in the xylene isomerization over H-mordenite (MOR) and demonstrated that the monomolecular 1,2-methyl shift pathway is prevailing because of the steric constraints within the 12-ring channels in H-mordernite.[22,23,25] Clark et al. have theoretically investigated the *m*-xylene disproportionation over zeolite Y (FAU), mordenite, and ZSM-5 and found that not only transition state shape selectivity but also product shape one plays a critical role in determining the distribution of 1,2,4-, 1,2,3-, and 1,3,5-trimethylbenzene (TMB) isomers.[26,27] Demuth et al. have also calculated the relative formation energies of reaction intermediates in the monomolecular 1,2-methyl shift and bimolecular DPM-mediated mechanisms of *m*-xylene disproportionation over theta-1 (TON) and mordenite. They have reported that the monomolecular pathway is far less sensible to the size of zeolite pores than the bimolecular one.[28] To our knowledge, however, no theoretical studies have focused on both isomerization and disproportionation of *m*-xylene over zeolite catalysts simultaneously and thus on both 3mDPM and 4mDPM species as reaction intermediates.

There are a total of 18 3mDPM and 21 4mDPM isomers with different molecular dimensions that can be formed as reaction intermediates of *m*-xylene disproportionation followed by transalkylation. Among them, however, only three 3mDPM and six 4mDPM isomers, as shown in Figure 1, can produce

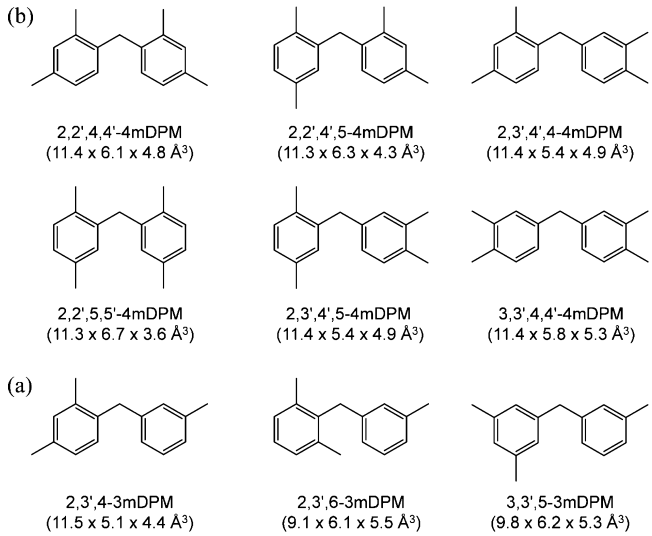

Figure 1. (a) Three 3mDPM and (b) six 4mDPM derivatives that can produce 1,2,4-TMB, the major product of *m*-xylene disproportionation. Their molecular dimensions in the gas state were calculated at the ωB97XD/6-31G(d) level.

1,2,4-TMB, the major product of *m*-xylene disproportionation, through their split-off.[15] In the present study, therefore, we calculate the strain energies of these nine bicyclic aromatic species in eight zeolites with different framework structures representing the four subgroups of medium-pore zeolites described above, as well as in the large-pore zeolite Y, in order to better understand the effects of zeolite pore structure on the mechanisms of the zeolite-catalyzed isomerization and disproportionation of

dx.doi.org/10.1021/cs500186y | ACS Catal. 2014, 4, 1764−1776

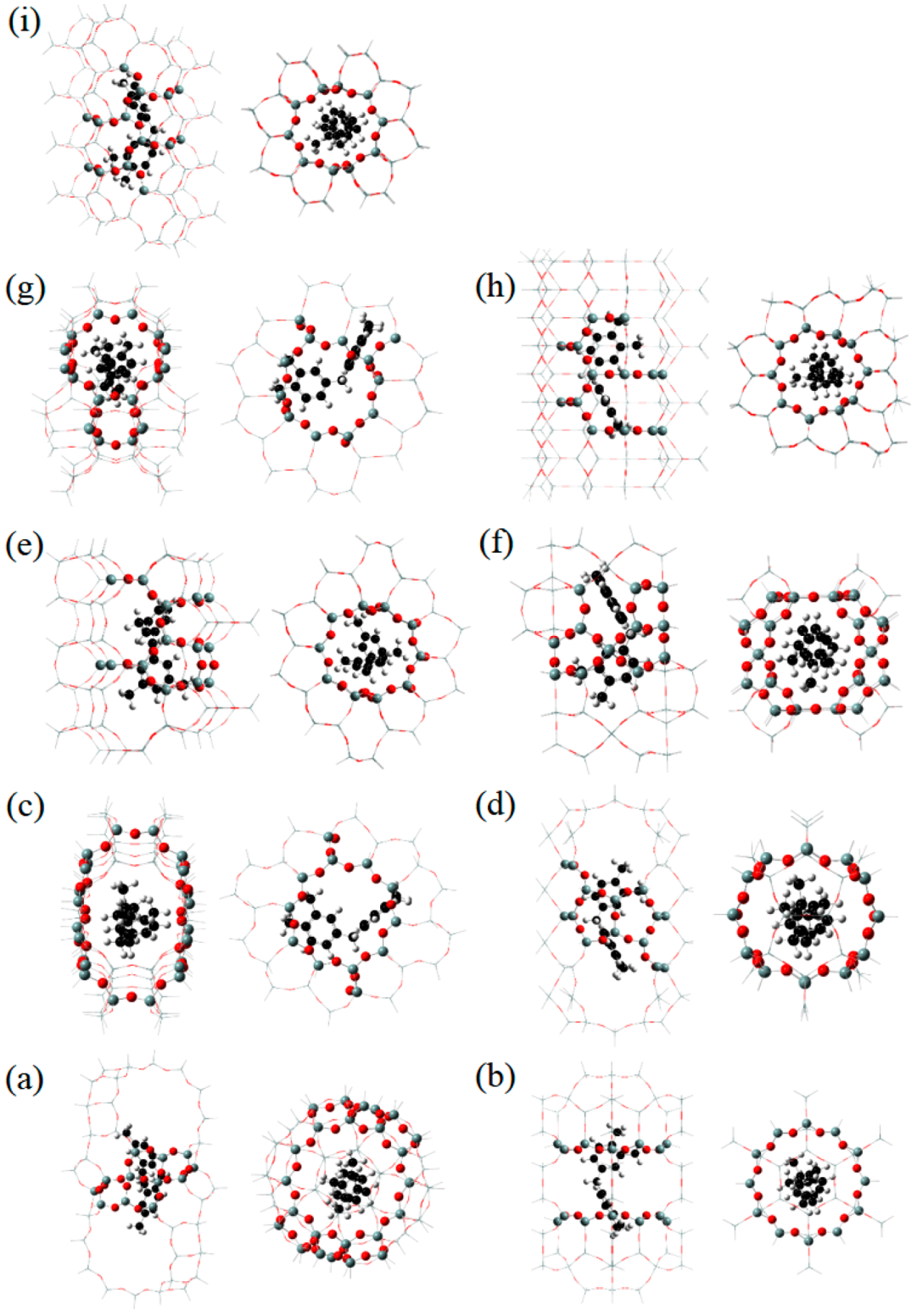

Figure 2. Side (left) and top (right) views of the structures of 2,2′,4,6′-4mDPM embedded in nine zeolites with different framework topologies optimized at the ONIOM (ωB97XD/6-31G(d):MNDO) level of theory: (a) zeolite Y, (b) MCM-22, (c) TNU-9, (d) NU-87, (e) ZSM-5, (f) ZSM-57, (g) TNU-10, (h) ZSM-22, and (i) ZSM-23.

m-xylene. We also calculate the relative energies of all species involved in the bimolecular isomerization and disproportionation of *m*-xylene over zeolite Y, TNU-9, and ZSM-23 which show notable differences in the pore topology. The calculation results obtained in this work are compared with the experimental ones recently reported by us.[15]

COMPUTIONAL METHODS

The 84T, 96T, 64T, 62T, 72T, 121T, 70T, 126T, and 142T cluster models, which were extracted from their crystallographic data,[31] were used to calculate the strain energies of 3mDPM and 4mDPM derivatives in zeolite Y, MCM-22, TNU-9, NU-87, ZSM-5, ZSM-57, TNU-10, ZSM-22, and ZSM-23, respectively.

dx.doi.org/10.1021/cs500186y | ACS Catal. 2014, 4, 1764−1776

Table 1. Structural Features of Zeolites with Different Framework Topologies Employed in This Study

zeolite	IZA code	pore topology	pore size[a] (Å)	D_i[b] (Å)
zeolite Y	FAU	3D, 12-ring	7.4 × 7.4	11.18
MCM-22	MWW	2D, 10-ring + large cages	4.0 × 5.5, 4.1 × 5.1	9.63
TNU-9	TUN	3D, 10-ring +12-ring cavities	5.5 × 5.6, 5.4 × 5.5	8.40
NU-87	NES	2D, 10- and 12-rings	4.8 × 5.7, 5.3 × 7.8[c]	6.98
ZSM-5	MFI	3D, 10-ring	5.1 × 5.5, 5.3 × 5.6	6.30
ZSM-57	MFS	2D, 10- and 8-rings	5.1 × 5.4 (3.3 × 4.8)	6.75
TNU-10	STI	2D, 10- and 8-rings	4.7 × 5.0 (2.7 × 5.6)	6.23
ZSM-22	TON	1D, 10-ring	4.6 × 5.7	5.65
ZSM-23	MTT	1D, 10-ring	4.5 × 5.2	6.13

[a]The values in parentheses are the size of 8-ring channels in the corresponding zeolite structure. [b]The maximum included sphere diameter defined as the diameter of the largest sphere among the spheres that could be included within intracrystalline void spaces, whereas their radii are the same as the distances between an arbitrary point in such spaces and its closest framework atom. For details, see ref 47. [c]12-Ring pore size.

As shown in Figure 2, these models include the complete pore structures of the corresponding zeolites so that the confinement effects on the reaction intermediates of *m*-xylene isomerization and disproportionation could be rationally considered. It is worth noting that more than two layers of the zeolite framework can be deformed when bimolecular 3mDPM or 4mDPM species are introduced. In this study, however, we considered only one layer of the zeolite framework in order to reduce the computational cost. It has been repeatedly shown that this approach is good enough to give theoretical results which are in excellent agreement with experimental ones.[26,27,34,35] The 84T, 64T, and 142T models were also used to calculate the relative energies of the reactant, reaction intermediates, transition states, and products of *m*-xylene isomerization and disproportionation over zeolite Y, TNU-9, and ZSM-23, respectively.

The theoretical hybrid model (i.e., a combination of ωB97XD/6-31G(d) and B3LYP/6-31G(d,p) methods with a semiempirical MNDO level) was employed in all calculations. The terminal Si atoms at each cluster edge were capped with H atoms at a Si−H bond length of 1.47 Å oriented along the direction of the corresponding Si−O bond. Although each adsorbed molecule, as well as a portion of the zeolite framework, was handled using a reliable density functional theory (DFT), the less demanding remainder of framework T atoms were treated at the MNDO level using the Gaussian 09 software package.[32] The ONIOM (ωB97XD/6-31G(d):MNDO) level of theory, where the ωB97XD function is the hybrid meta DFT developed by Chai

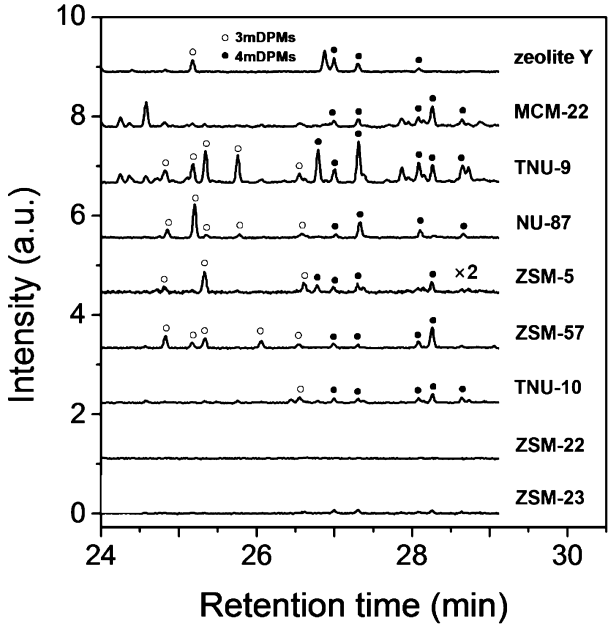

Figure 3. GC-MS total ion chromatograms of the CH_2Cl_2 extracts from nine zeolites with different framework structures after the isomerization and disproportionation of *m*-xylene at 523 K and 5.2 h^{-1} WHSV. Adapted from ref 15.

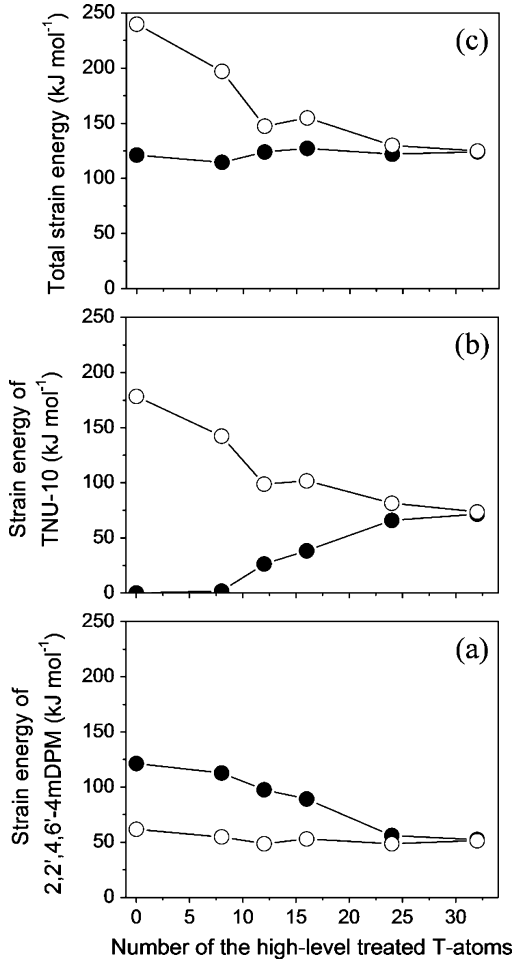

Figure 4. Strain energy of (a) 2,2′,4,6′-4mDPM in the gas state and of (b) the TNU-10 framework itself and (c) total strain energy of 2,2′,4,6′-4mDPM in TNU-10 vs number of high-level treated T atoms. Closed and open circles indicate the numbers of T atoms fixed and relaxed at the ωB97XD/6-31G(d,p) level, respectively.

dx.doi.org/10.1021/cs500186y | ACS Catal. 2014, 4, 1764−1776

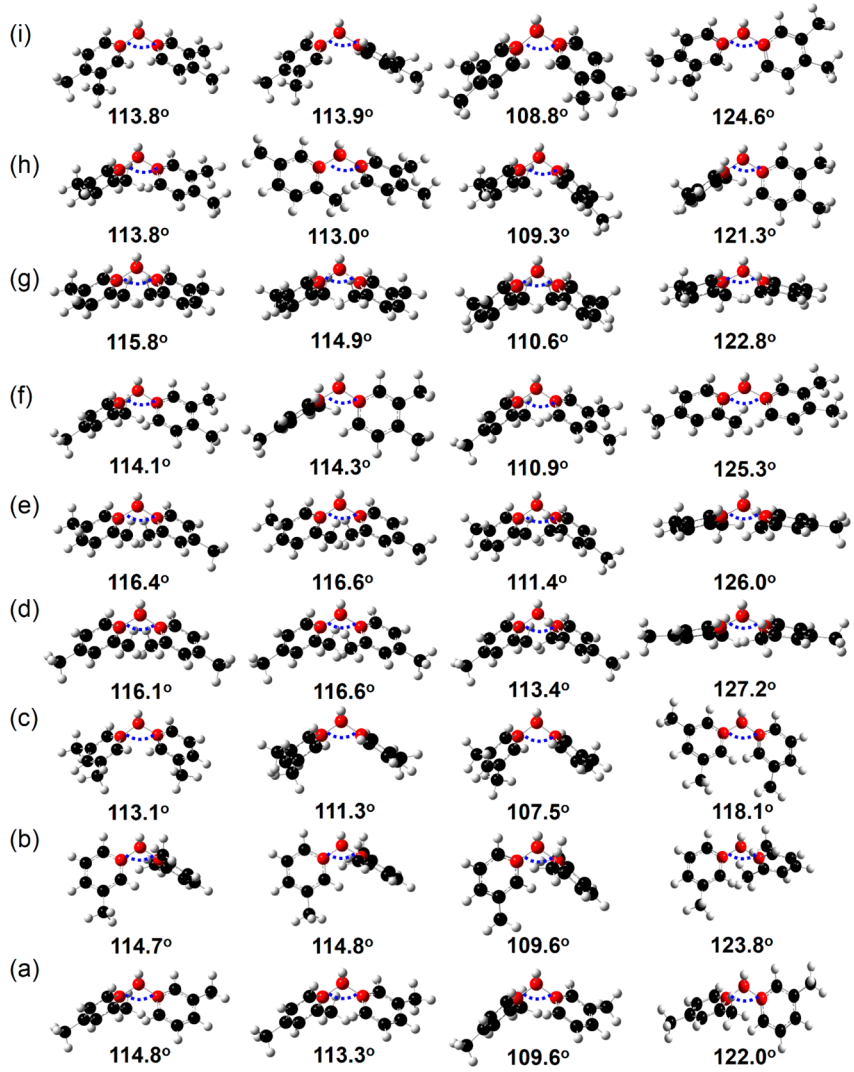

Figure 5. Structures of (a) 2,3′,4-3mDPM, (b) 2,3′,6-3mDPM, (c) 3,3′,5-3mDPM, (d) 2,2′,4,4′-4mDPM, (e) 2,2′,4′,5-4mDPM, (f) 2,3′,4′,4-4mDPM, (g) 2,2′,5,5′-4mDPM, (h) 2,3′,4′,5-4mDPM, and (i) 3,3′,4,4′-4mDPM in the gas state (1st column) and in zeolite Y (2nd column), TNU-9 (3rd column), and ZSM-23 (4th column). The angles of their central sp^3 carbons are also given. The zeolite framework was removed after structural optimization at the ONIOM (ωB97XD/6-31G(d):MNDO) level.

and Head-Gordon,[33] was applied to optimize the geometries of intrazeolitic 3mDPM and 4mDPM derivatives. It has been repeatedly shown that this level describes the long-range dispersive interactions between the adsorbate and zeolite framework better than the traditional DFT methods, allowing the calculated strain energies to correlate nicely with the experimental results.[34,35] During the geometric optimization, in general, the 24 T atoms surrounding the adsorbed molecule within the zeolite framework, as well as the adsorbed molecule itself, were treated at the high ωB97XD level. The rest of T atoms in the theoretical model were treated at the low MNDO level and kept fixed at their crystallographic positions. The single-point energy calculations were further refined at the ωB97XD/6-31G(d,p) level using the optimized structures. Frequency calculations were not carried out here because of the high computational cost.

Unlike the case of strain energy calculations, the ONIOM (B3LYP/6-31G(d,p):MNDO) level of theory was applied to calculate the relative energies of all species that can be formed during the bimolecular isomerization and disproportionation of *m*-xylene over some zeolites. Although the ωB97XD functional is more effective for describing the long-range dispersive interactions between the adsorbate and zeolite framework than the B3LYP one, the latter functional has also proved to accurately predict the structures of adsorbed hydrocarbon molecules in zeolites and their relative energies.[26,27] The organic molecule and the 8 T atoms in the zeolite framework surrounding the adsorbed species were treated at a high level and allowed to relax during the geometric optimization.

The adsorption energies of adsorbed molecules in zeolites are derived from a combination of two contributions: one due to the hydrogen bonds and dispersive interactions with the zeolite framework and the other due to the deformation of both adsorbate and zeolite framework.[34,36] The total strain and adsorption energies are therefore

$$E_{str} = \Delta E_{str}^{ads} + \Delta E_{str}^{zeo} \quad (1)$$

$$\Delta E_{ads} = \Delta E_{int} + E_{str} \quad (2)$$

where ΔE_{str}^{ads} and ΔE_{str}^{zeo} are the strain energies of the adsorbate and the zeolite framework, respectively, and ΔE_{int} is the interaction energy between them. ΔE_{int}, ΔE_{str}^{ads}, and ΔE_{str}^{zeo} are

dx.doi.org/10.1021/cs500186y | ACS Catal. 2014, 4, 1764−1776

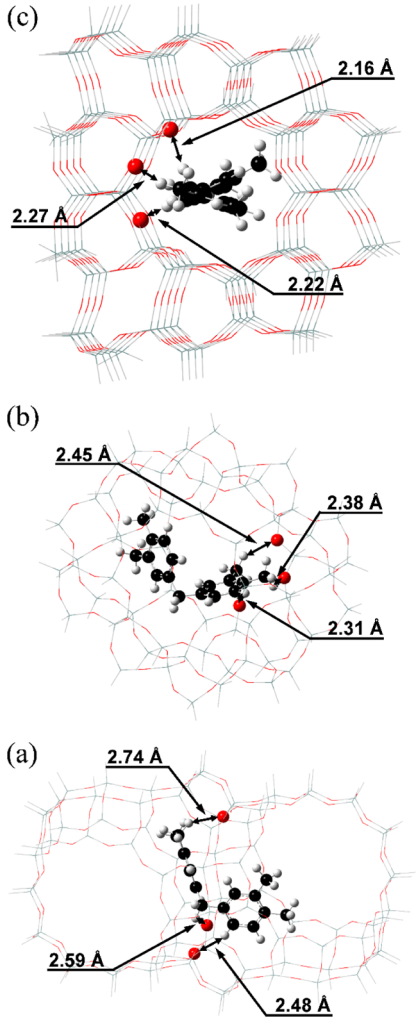

Figure 6. Structures of 3,3′,4,4′-4mDPM in (a) zeolite Y, (b) TNU-9, and (c) ZSM-23 optimized at the ONIOM (ωB97XD/6-31G(d):MNDO) level.

$$\Delta E_{\text{int}} = E_{\text{complex}} - E^{\text{c}}_{\text{zeolite}} - E^{\text{c}}_{\text{adsorbate}} \quad (3)$$

$$\Delta E^{\text{ads}}_{\text{str}} = E^{\text{c}}_{\text{adsorbate}} - E_{\text{adsorbate}} \quad (4)$$

$$\Delta E^{\text{zeo}}_{\text{str}} = E^{\text{c}}_{\text{zeolite}} - E_{\text{zeolite}} \quad (5)$$

where E_{complex} is the energy of the adsorption complex consisting of the adsorbate and the zeolite framework. Also, $E^{\text{c}}_{\text{adsorbate}}$ and $E^{\text{c}}_{\text{zeolite}}$ are the energies of the adsorbate and the zeolite framework, respectively, extracted from the adsorption complex without further optimization.

RESULTS AND DISCUSSION

Experimental Background. Table 1 shows the structural features of all zeolites employed in this work, and Figure 3 compares the GC-MS total ion chromatograms of CH_2Cl_2 extract from eight different zeolites representing the four subgroups of medium-pore zeolite catalysts classified by the structural criteria stated above, as well as from the large-pore zeolite Y, after the *m*-xylene isomerization and disproportionation at 523 K for 30 h on stream, which were adapted from ref 15. It can be seen that the number and relative intensity of the observed 3mDPM and 4mDPM GC-MS signals vary significantly with the size, shape, and/or dimensionality of zeolitic void spaces. For example, five, three, and two 3mDPM signals are observable in the GC-MS chromatograms from H-TNU-9, H-ZSM-5, and H−Y, respectively. However, no detectable signals were found in the chromatograms from H-ZSM-22 and H-ZSM-23 with narrower 1D 10-ring (4.6 × 5.7 and 4.5 × 5.2 Å, respectively) channels. This clearly shows that the pore structure of medium-pore zeolites is a crucial factor governing the mechanisms of *m*-xylene isomerization and disproportionation.

Effect of Zeolite Framework Deformation on the Strain Energy. In general, the zeolite framework is deformed when the guest molecules are adsorbed.[35] If all atoms in the theoretical model are relaxed during the optimization process, this would then be an ideal case. A serious problem of this approach is that in addition to its quite high computational cost, the unique structural features of each zeolite cannot be preserved during the strain energy calculations.[34] Therefore, a portion of the zeolite framework T atoms, together with the adsorbed molecule, should be treated at a high level.[37−44] In fact, we found that the strain energy of the adsorbate is strongly altered according to the number of high-level relaxed T atoms (see below).

To investigate the effects of the number of high-level relaxed T atoms on the strain energies of the adsorbate and zeolite framework, as well as on their total strain energies, we have selected 2,2′,4,6′-4mDPM and TNU-10 as the model reaction intermediate and the model zeolite framework, respectively. Although the split-off of 2,2′,4,6′-4mDPM can produce *m*-xylene and 1,2,4-TMB, the reactant and the major product of this aromatic conversion, respectively, medium-pore zeolites with intersecting 10- and 8-ring channels like TNU-10 have a greater influence on the structure of bicyclic aromatic reaction intermediates than those containing cavities/channels larger than 10-ring pores. Furthermore, H-TNU-10 was found to be more selective to *p*-xylene formation than H-ZSM-5, one of the commercial xylene isomerization catalysts.[15] By contrast, the structure of such bulky molecules can be excessively modified upon adsorption on zeolites with narrow 1D 10-ring channels only. In this subsection, we will refer to all strain energies as their abbreviations ($\Delta E^{\text{zeo}}_{\text{str}}$, $\Delta E^{\text{ads}}_{\text{str}}$, and E_{str}) in order to avoid any possible confusion. After relaxing all T atoms at the low MNDO level, the number of T atoms treated at the high ωB97XD level increased gradually from zero to 32. Then, we calculated $\Delta E^{\text{zeo}}_{\text{str}}$, $\Delta E^{\text{ads}}_{\text{str}}$, and E_{str} while fixing the rest of T atoms at the low MNDO level in the TNU-10 framework at the same level of theory. All capped H atoms at the cluster edge were fixed during the calculations, and the structures of 2,2′,4,6′-4mDPM in TNU-10 with different numbers of T atoms relaxed at the ONIOM (ωB97XD/6-31G(d):MNDO) level can be found in Supporting Information Figure S1.

As shown in Figure 4, $\Delta E^{\text{ads}}_{\text{str}}$ was calculated to be 62 kJ mol^{-1} when all T atoms are relaxed at a low level. No noticeable changes in the $\Delta E^{\text{ads}}_{\text{str}}$ value were caused by increasing the number of high-level treated T atoms from zero to 32. As this number increased up to 12, $\Delta E^{\text{zeo}}_{\text{str}}$ decreased dramatically from 178 to 99 kJ mol^{-1}. A quite similar trend was also observed for E_{str}. However, a further increase of high-level treated T atoms to 32 gave no significant changes in the $\Delta E^{\text{zeo}}_{\text{str}}$ or E_{str} value. When most of the zeolite framework T atoms are treated at a high level during the geometric optimization, therefore, $\Delta E^{\text{ads}}_{\text{str}}$ appears to become practically independent of the number of high-level treated T atoms. This is not unexpected because the dispersive interactions associated with zeolite framework deformation have already been reflected on the intrazeolitic structure of the adsorbate. However, if the number of high-level treated T atoms were smaller than the critical value, the extent of zeolite framework deformation should

dx.doi.org/10.1021/cs500186y | ACS Catal. 2014, 4, 1764−1776

Table 2. Strain, Interaction, and Adsorption Energies of Three 3mDPM and Six 4mDPM Isomers Embedded in Zeolites with Different Framework Topologies Calculated at the ωB97XD/6-31G(d,p) Level of Theory

		strain, interaction, and adsorption energy (kJ mol^{-1})								
		3mDPM and 4mDPM derivatives								
zeolite		2,3′,4-3mDPM	2,3′,6-3mDPM	3,3′,5-3mDPM	2,2′,4, 4′-4mDPM	2,2′,4′,5-4mDPM	2,3′,4′,4-4mDPM	2,2′,5,5′-4mDPM	2,3′,4′,5-4mDPM	3,3′,4,4′-4mDPM
zeolite Y	[a] ΔE_{str}^{ads}	1	2	3	2	1	4	2	4	3
	[b] ΔE_{str}^{zeo}	1	5	2	1	1	4	3	5	4.5
	[c] E_{str}	2	7	5	2	3	8	4	9	7
	[d] ΔE_{int}	−126	−141	−130	−134	−142	−131	−145	−135	−132
	[e] ΔE_{eds}	−124	−134	−125	−131	−139	−122	−141	−126	−124
MCM-22	ΔE_{str}^{ads}	4	1	3	3	4	5	4	4	5
	ΔE_{str}^{zeo}	2	1	1	2	3	2	2	2	1
	E_{str}	6	3	4	5	6	7	6	6	6
	ΔE_{int}	−130	−112	−120	−128	−139	−138	−138	−139	−133
	ΔE_{eds}	−123	−109	−116	−123	−133	−131	−132	−133	−127
TNU-9	ΔE_{str}^{ads}	6	13	10	3	7	5	7	13	11
	ΔE_{str}^{zeo}	1	2	3	−1	1	1	1	1	2
	E_{str}	8	15	13	3	8	5	8	14	13
	ΔE_{int}	−156	−132	−133	−176	−165	−176	−176	−171	−156
	ΔE_{eds}	−148	−117	−120	−173	−157	−172	−168	−157	−143
NU-87	ΔE_{str}^{ads}	9	21	7	21	26	33	28	27	8
	ΔE_{str}^{zeo}	2	20	7	7	6	6	5	5	4
	E_{str}	12	41	14	27	32	38	33	32	12
	ΔE_{int}	−171	−84	−156	−148	−158	−149	−158	−153	−179
	ΔE_{eds}	−159	−43	−142	−121	−126	−111	−126	−121	−167
ZSM-5	ΔE_{str}^{ads}	14	34	14	87	114	44	67	133	74
	ΔE_{str}^{zeo}	19	13	8	44	25	23	25	25	43
	E_{str}	33	47	22	131	139	68	92	158	117
	ΔE_{int}	−143	−96	−186	23	−47	−57	−60	15	62
	ΔE_{eds}	−110	−49	−165	154	92	10	32	173	180
ZSM-57	ΔE_{str}^{ads}	18	35	54	46	33	33	19	27	9
	ΔE_{str}^{zeo}	16	25	57	19	23	18	17	20	15
	E_{str}	34	59	111	65	55	51	37	47	25
	ΔE_{int}	−152	−131	55	−146	−160	−137	−168	−141	−218
	ΔE_{eds}	−118	−72	167	−82	−104	−86	−132	−94	−194
TNU-10	ΔE_{str}^{ads}	30	36	39	35	73	12	43	67	36
	ΔE_{str}^{zeo}	15	23	31	70	30	18	38	47	15
	E_{str}	45	59	70	105	102	30	81	113	51
	ΔE_{int}	−152	−115	−78	−61	−50	−201	−82	−65	−164
	ΔE_{eds}	−107	−56	−8	43	53	−171	−1	48	−113
ZSM-22	ΔE_{str}^{ads}	79	69	47	66	60	61	73	105	98
	ΔE_{str}^{zeo}	59	60	36	37	40	38	35	59	47
	E_{str}	138	129	83	103	99	98	108	164	145
	ΔE_{int}	9	−36	−109	−111	−91	−122	−24	32	−11
	ΔE_{eds}	148	93	−26	−8	8	−24	83	196	134
ZSM-23	ΔE_{str}^{ads}	19	60	48	54	50	44	45	44	58
	ΔE_{str}^{zeo}	47	45	59	43	42	44	24	66	61
	E_{str}	66	104	107	96	93	88	69	110	118
	ΔE_{int}	−131	−26	−15	−100	−93	−80	−92	−37	−74
	ΔE_{eds}	−65	78	91	−4	−1	8	−23	73	44

[a] $\Delta E_{str}^{ads} = E_{adsorbate}^{c} - E_{adsorbate}$. [b] $\Delta E_{str}^{zeo} = E_{zeolite}^{c} - E_{zeolite}$. [c] $E_{str} = \Delta E_{str}^{ads} + \Delta E_{str}^{zeo}$. [d] $\Delta E_{int} = E_{complex} - E_{zeolite}^{c} - E_{adsorbate}^{c}$. [e] $\Delta E_{ads} = \Delta E_{int} + E_{str}$.

then be influenced strongly by the volume of adsorbed molecules, yielding notable changes in the ΔE_{str}^{zeo} value.

Figure 4 also shows that when most of the framework T atoms were fixed and treated at a high level, ΔE_{str}^{ads} decreased gradually from 121 to 56 kJ mol^{-1} with increasing the number of high-level treated T atoms up to 24 and remained almost unchanged at a larger number of 32. However, ΔE_{str}^{zeo} began to increase at a number of 8 and became 72 kJ mol^{-1} at the final number of 32. We should note here that as the numbers of fixed and relaxed T atoms at a high level increased, respectively, all the ΔE_{str}^{zeo}, ΔE_{str}^{ads}, and E_{str} values were converged on the particular values because of the size of the adsorbed molecule. Thus, the deformed area of the zeolite framework should differ according to the size of the adsorbed organic species. Of particular interest is that when most of framework T atoms were fixed, E_{str} remained almost unchanged over the number range for high-level treated T atoms

dx.doi.org/10.1021/cs500186y | ACS Catal. 2014, 4, 1764−1776

studied here and was practically identical with the value calculated using the high-level relaxed zeolite framework. This indicates that the E_{str} value calculated using the fixed zeolite framework is also reliable, regardless of the number of high-level relaxed T atoms utilized in calculations. Apparently, the use of the fixed zeolite framework instead of the relaxed one in the strain energy calculations can reduce the computational cost largely. However, Figure 4 shows that at least 24 T atoms need to be relaxed at a high level to obtain reliable ΔE_{str}^{zeo} and ΔE_{str}^{ads} values. In this study, therefore, we have relaxed 24 T atoms of each zeolite framework while fixing the rest of its T atoms at a low level.

Strain Energies of 3mDPM and 4mDPM Derivatives in Zeolites with Different Framework Topologies. Figure 5 shows the structures of three 3mDPM and six 4mDPM isomers studied in this work, which were optimized at the ωB97XD/6-31G(d) level, with and without the zeolite Y, TNU-9, or ZSM-23 framework present. Their central sp^3 carbon bond angles (C−C−C angle) in these three zeolites, as well as in the gas state, are given in Supporting Information Table S1. The angles of their central sp^3 carbons when present in the gas state were calculated to be in the range of 113.1−116.4°. These values are larger by 3.6−6.9° than the ideal angle (109.5°) of sp^3 hybridization,[45] probably due to the steric hindrance of two neighboring phenyl groups. As shown in Figure 5, however, the sp^3 carbon bond angles of 3mDPM and 4mDPM derivatives in zeolite Y deviate slightly from those of the corresponding aromatic compounds in the gas state: differences are not larger than 1.6°. The structure of 3,3′,4,4′-4mDPM, which has the largest dimensions among the 3mDPM and 4mDPM species in Figure 1, located within the supercages in zeolite Y through the van der Waals (vdW) interactions is shown in Figure 6. All H atoms in this 4mDPM derivative were calculated to be farther than 2.48 Å from the zeolite framework, indicating the weak nature of their interactions. Given that the supercages with a diameter of 13.0 Å in zeolite Y, connected with one another via 12-ring (7.4 × 7.4 Å) windows, are large enough to accommodate 3,3′,4,4′-4mDPM, this is reasonable.

The structural results in Figures 5 and 6 also reveal that although the central sp^3 carbon bond angles of 3mDPM and 4mDPM derivatives in TNU-9 deviate by 3.2−8.6° compared with those of the corresponding compounds in the gas state, all H atoms in 3,3′,4,4′-mDPM are farther than 2.31 Å from the TNU-9 framework. This medium-pore zeolite has two slightly wider and narrower 10-ring (5.5 × 5.6 and 5.1 × 5.5 Å) channels down the *b*-axis, together with the 12-ring cavities with dimensions of 5.3 × 10.9 × 15.7 Å limited by the wider channel down the *b*-axis and by the short bridging 10-ring channel in the third direction.[46] When the 3mDPM and 4mDPM species are introduced within ZSM-23 with a 1D 10-ring channel system, the range (5.3−11.2°) of deviation of their sp^3 carbon bond angles with respect to the gas state becomes larger again. Also, the closest distance between the H atoms in 3,3′,4,4′-mDPM and this zeolite framework is 2.16 Å. As expected, therefore, it is clear that the extent of deformation of 3mDPM and 4mDPM derivatives upon their adsorption on zeolites becomes more severe within zeolites with narrower void spaces.

To obtain more quantitative evidence that supports the above conclusion, we calculated the strain energies of three 3mDPM and six 4mDPM isomers in eight medium-pore zeolites with different pore structures, as well as in zeolite Y. As listed in Table 2, their strain energies in zeolite Y, TNU-9, and MCM-22, all of which contain large cavities are always lower than ca. 9, 15, and 7 kJ mol^{-1}, respectively. When embedded in ZSM-5 free of such large cavities, however, 3mDPM and 4mDPM species are characterized by considerably higher strain energies (21−47 and 67−158 kJ mol^{-1}, respectively). Moreover, their strain energies in ZSM-22 and ZSM-23 are higher than 65 kJ mol^{-1}, suggesting that the formation of bicyclic aromatic molecules in these zeolites with narrow 1D 10-ring channels are severely limited due to steric hindrance, in excellent agreement with the GC-MS results in Figure 3.

Very recently, Willems et al. have demonstrated that the maximum included sphere diameter (D_i), which is defined as the diameter of the largest sphere among the spheres that could be included within intracrystalline void spaces, while their radii are the same as the distances between an arbitrary point in such spaces and its closest framework atom, is an efficient geometrical parameter for quantitatively describing the channel/cavity of crystalline porous materials such as zeolites, metal organic materials, and zeolitic imidazolate frameworks.[47] This has led us to pay attention to the relationship of the D_i value of zeolites with different framework topologies employed in our work with the extent of deviation of the central sp^3 carbon bond angles and the strain energy of 3mDPM and 4mDPM derivatives embedded in the corresponding zeolites. As shown in Figure 7, the extents of deviation of the sp^3 carbon angles are somewhat larger for 4mDPM species than for 3mDPM ones. This is not strange

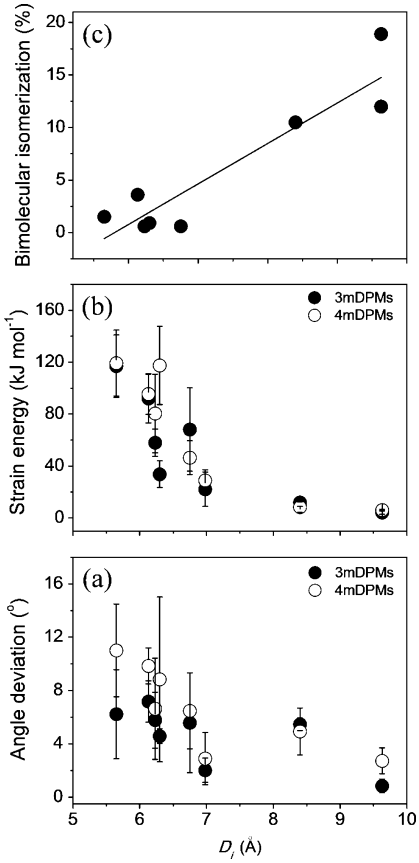

Figure 7. (a) Extent of deviation of the central sp^3 carbon bond angles and (b) strain energy of three 3mDPM and six 4mDPM isomers in eight medium-pore zeolites with different framework topologies and (c) percentage of bimolecular isomerization in the formation of *o*-xylene from *p*-xylene over the corresponding zeolites[15] vs maximum included sphere diameter (D_i)[44] of each medium-pore zeolite.

dx.doi.org/10.1021/cs500186y | ACS Catal. 2014, 4, 1764−1776

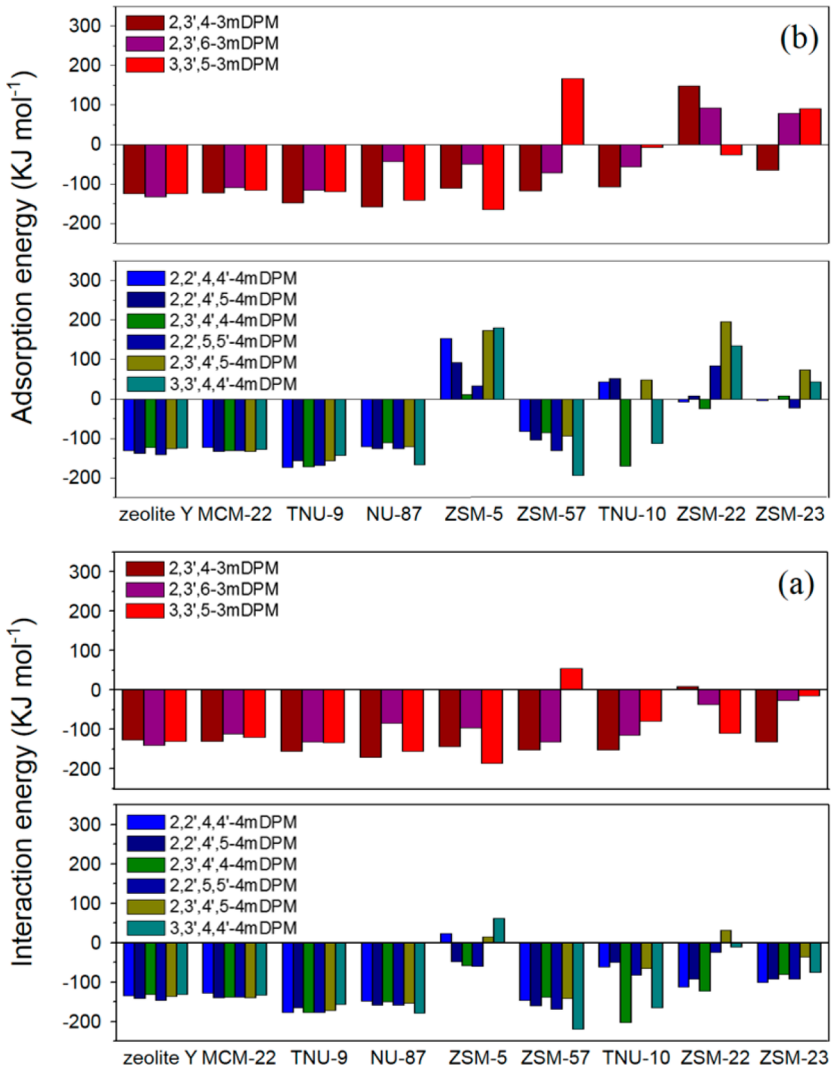

Figure 8. (a) Interaction and (b) adsorption energies of three 3mDPM and six 4mDPM isomers in nine zeolites with different framework topologies.

because the former aromatic compounds have one more methyl group and thus experience slightly more severe steric hindrance. An interesting observation is that the extents of angle deviation for both types of reaction intermediates increased suddenly at D_i values below 7.0 Å, which is also the case of their strain energies. One obvious reason for this may be that the dimensions of some 4mDPM derivatives (e.g., 3,3′,5-4mDPM and 2,2′,5,5′-4mDPM with dimensions of 6.2 × 5.3 Å and 6.7 × 3.6 Å along the *b*- and *c*-axes, respectively; Figure 1), are quite close to 7.0 Å.

Figure 7 also shows a plot of the D_i value of nine zeolites with different framework topologies used as *m*-xylene isomerization and disproportionation catalysts versus their percentage of bimolecular isomerization in the formation of *o*-xylene from *p*-xylene determined from isotope labeling experiments using an equimolar mixture of normal and hexadeuterated *p*-xylenes at 523 K.[15] It can be seen that zeolite catalysts with D_i < 7.0 Å exhibit negligible percentages (<4%) of bimolecular isomerization, although the percentage becomes considerably larger with increasing D_i. This suggests that zeolites with D_i values around 7.0 Å are situated at the threshold of the bimolecular reaction pathway of *m*-xylene isomerization and disproportionation. There are at least eight medium-pore zeolites with $D_i \geq$ 7.0 Å (Supporting Information Table S2). Therefore, the prevailing mechanism of *m*-xylene conversion over medium-pore zeolites cannot always be regarded as monomolecular.

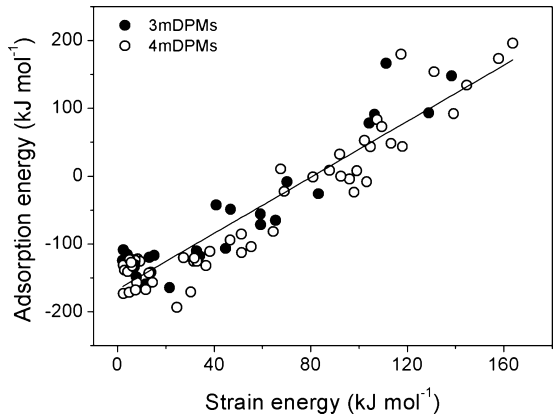

Figure 9. Adsorption energy of 3mDPM and 4mDPM derivatives in nine zeolites with different framework topologies vs their strain energy.

Figure 8 compares the interaction and adsorption energies of three 3mDPM and six 4mDPM isomers in nine different zeolites studied here. These data reveal that while most of them show positive adsorption energies in ZSM-22 and ZSM-23, all

dx.doi.org/10.1021/cs500186y | ACS Catal. 2014, 4, 1764−1776

derivatives are characterized by negative ones in zeolite Y, TNU-9, and MCM-22. A positive linear relationship is observed when the adsorption energies in Figure 8 are plotted against their corresponding strain ones (Figure 9). Therefore, it is most likely that the size of void spaces in medium-pore zeolites governs the extent (i.e., strain energy) of deformation of bicyclic aromatic reaction intermediates formed during the isomerization and disproportionation of *m*-xylene and then their adsorption energies. The strain energies of three 3mDPM and six 4mDPM isomers in a series of zeolites with different framework topologies are compared in Figure 10. The strain energies of all

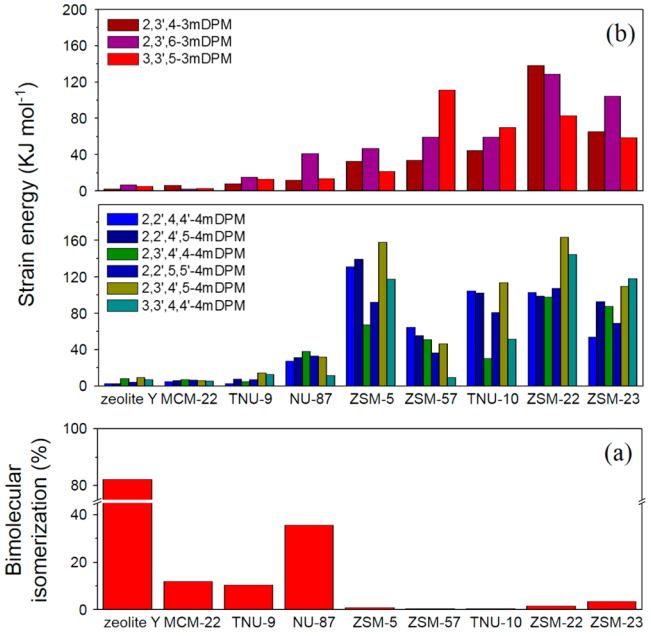

Figure 10. (a) Percentages of bimolecular isomerization in the formation of *o*-xylene from *p*-xylene over nine zeolites with different framework topologies[15] and (b) strain energies of three 3mDPM and six 4mDPM isomers in the corresponding zeolites.

the bicyclic reaction intermediates in zeolite Y with a degree of bimolecular isomerization of 82% were calculated to be lower than 19 kJ mol^{-1}, suggesting the ease of their formation. When embedded in MCM-22, TNU-9, and NU-87 containing 12-ring cavities/channels, on the other hand, their energies became higher (<40 kJ mol^{-1}). Also, some 3mDPM and 4mDPM derivatives in cavity-free ZSM-5, ZSM-57, and TNU-10 are characterized by the strain energies considerably higher than 40 kJ mol^{-1}. In particular, all species in ZSM-22 and ZSM-23 with narrower 1D 10-ring channels gave much higher strain energies. These results are inversely correlated well with the percentages of bimolecular isomerization in the formation of *o*-xylene from *p*-xylene over different medium-pore zeolites.[15]

Relative Energies of All Species Involved in the Bimolecular Isomerization and Disproportionation of *m*-Xylene. Figure 11 shows the relative energy level diagram for the reactant, reaction intermediates, and transition states of the bimolecular isomerization and disproportionation of *m*-xylene over zeolite Y, and Table 3 lists their relative energies. Although the zeolite Y structure has only one crystallographically distinct T-site, there are four crystallographically distinct O sites at which the proton can be located upon Al substitution (Supporting Information Figure S2). From a thermodynamic point of view, site O4 is the most stable O site so that the adsorbed *m*-xylene

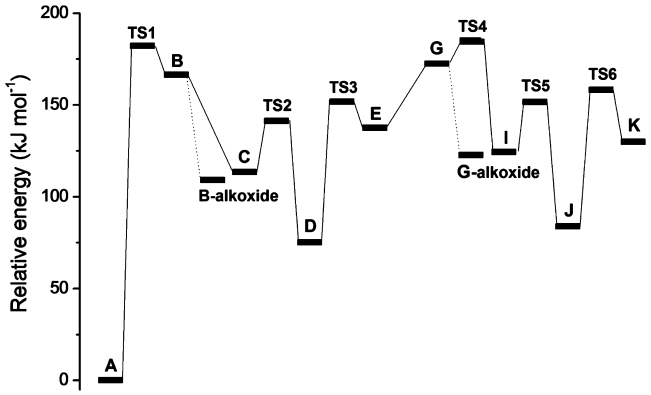

Figure 11. Relative energy level diagram for the reactant, reaction intermediates, and transition states of the bimolecular isomerization and disproportionation of *m*-xylene over zeolite Y.

molecule can be easily changed to its alkoxide form.[26] In the relative energy calculations, therefore, this O site was selected as the proton location of Brønsted acid sites in zeolite Y. Also, all the energies in Table 3 are referenced relative to the energy of "the three *m*-xylene molecules embedded in zeolite Y" which logically satisfy the bimolecular reaction pathway in Scheme 1. Among the bicyclic aromatic species in Figure 3, 3,3′,5-3mDPM and 2,2′,4,5′-4mDPM were adapted as the main reaction intermediates of both disproportionation and transalkylation cycles in Scheme 1, respectively. This is because their split-off produces *p*-xylene and 1,2,4-TMB, respectively, the major products of *m*-xylene conversion over most medium-pore zeolites we have recently studied.[15]

Clark et al. have previously shown that the formation of the *m*-tolylmethylium cation (**B**) by hydride abstraction has the highest energy barrier (206 kJ mol^{-1}) among the elementary steps of *m*-xylene disproportionation over zeolite Y.[27] In our work, the energy barrier (TS1) to the formation of this cation was calculated to be 183 kJ mol^{-1}. While this value is still highest among all the elementary steps in Scheme 1, the discrepancy with our results can be attributed to the difference in theoretical model of zeolite Y: our theoretical model includes two supercages, whereas there is only one supercage in the model of Clark et al. As described above, on the other hand, species **B** or its alkoxide form can be converted to the benzenium-type carbenium ion (**C**) by reacting with another *m*-xylene. Then, species **C** must overcome two energy barriers or transition states (denoted TS2 and TS3) to produce toluene (**F**) and the (dimethylphenyl)-methylium ion (**G**). TS2 was calculated to have an energy barrier of 28 kJ mol^{-1}. The structure of this transition state can be found in Supporting Information Figure S3. The proton is located in the middle of the C atom of the aromatic ring with a bond distance of 1.41 Å and the O atom in the zeolite framework with a bond distance of 1.30 Å. To further advance the disproportionation of *m*-xylene, the proton of the Brønsted acid sites in zeolite Y must be migrated to the other aromatic ring of a neutral 3mDPM species (i.e., 3,3′,5-3mDPM). As shown in Table 3, however, this proton transfer (TS3) was found to have the highest energy barrier (76 kJ mol^{-1}) among all the transition states except TS1 in Scheme 1. This led us to conclude that the proton migration from Brønsted acid sites to the neural aromatic species is thermodynamically less favorable than the reverse reaction.

It is also remarkable that the split-off of species **E** can yield six different types of (dimethylphenyl)methylium ions (i.e., **G**), as

dx.doi.org/10.1021/cs500186y | ACS Catal. 2014, 4, 1764−1776

Table 3. Relative Energies of the Reactant, Reaction Intermediates, Transition States, and Products of the Bimolecular Isomerization and Disproportionation of *m*-Xylene over Zeolite Y

species[a]	energy (kJ mol^{-1})	species[a]	energy (kJ mol^{-1})
three *m*-xylenes in zeolite Y	0	**G** alkoxide-1^{+},2,4-TMB	124
TS1	183	**G** alkoxide-1,2^{+},4-TMB	123
B	167	**G** alkoxide-1,2,4^{+}-TMB	123
B alkoxide	109	**G** alkoxide-1^{+},2,3-TMB	135
C	114	**G** alkoxide-1,2^{+},3-TMB	150
TS2	142	**G** alkoxide-1^{+},3,5-TMB	122
D	76	TS4	185
TS3	152	**I**	125
E	138	TS5	152
G-1^{+},2,4-TMB	160	**J**	85
G-1,2^{+},4-TMB	173	TS6	155
G-1,2,4^{+}-TMB	167	**K**	130
G-1^{+},2,3-TMB	190	*p*-xylene and 1,2,4-TMB	2
G-1,2^{+},3-TMB	183	*p*-xylene and 1,3,5-TMB	1
G-1^{+},3,5-TMB	175	*p*-xylene and 1,2,3-TMB	9

[a]The same as those given in Scheme 1.

well as **F**, depending on the position of proton abstraction in each of three TMB isomers (Supporting Information Figure S4). The relative energy calculation results in Table 3 indicate that the four (dimethylphenyl)methylium ions generated from 1,2,4- and 1,3,5-TMB isomers have similar energy levels to one another. However, we found that the energy levels (183 and 190 kJ mol^{-1}, respectively) of the other two cations produced from 1,2,3-TMB are higher by at least 8 and 15 kJ mol^{-1} than those of the cations from 1,2,4- or 1,3,5-TMB, probably due to the steric hindrance of locally concentrated methyl branches. Upon their adsorption on the Brønsted acid sites, these cations are converted to the more stable alkoxide form as shown in Figure 11. The most interesting result obtained from Table 3 is that the energy barriers (<30 kJ mol^{-1}) to TS4 are much lower than the barrier (183 kJ mol^{-1}) of hydride abstraction and transfer from species **G** to **B**. When the **G**-1,2^{+},4-TMB cation with the highest relative energy (173 kJ mol^{-1}) among the cations yielding 1,2,4-TMB is selected, for example, the energy barrier to TS4 was calculated to be 12 kJ mol^{-1} only. This supports our recent proposal that the transalkylation cycle in Scheme 1 is thermodynamically favorable enough to operate by itself in order to produce a xylene mixture (**L**), although it cannot start without *m*-xylene disproportionation.[15]

Finally, we calculated the relative energies of reaction intermediates **I**−**K** in the transalkylation cycle in order to better understand the effects of zeolite pore structure on their formation. To save the computational cost, we selected only three zeolites (i.e., zeolite Y, TNU-9, and ZSM-23) but with notable differences in the pore size and/or dimensionality. Among the 24 and 7 crystallographically distinct T-sites in TNU-9 and ZSM-23, respectively, one Al atom was located at the T-site with the easiest access to 4mDPM species. The energy level diagram for species **I**−**K** in zeolite Y, TNU-9, and ZSM-23 are given in Figure 12, and their energies calculated relative to the (dimethylphenyl)methylium ion **G** are compared in Table 4. The relative energy of the cation **I** in zeolite Y was calculated to be −42 kJ mol^{-1}, which is even lower than the energy of the smaller species **G**. This implies that the supercages in zeolite Y are large enough to form 4mDPM derivatives without any severe steric constraints. However, the energy difference between species **I** and **G** in TNU-9 is only −4 kJ mol^{-1}. In particular, the difference in ZSM-23 is 153 kJ mol^{-1}, indicating much difficulty in the formation of bicyclic aromatic reaction

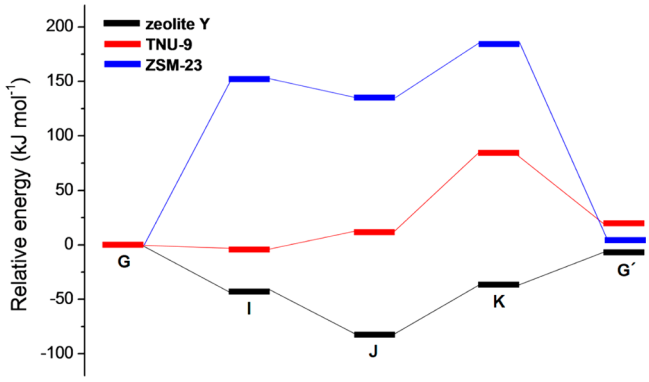

Figure 12. Relative energy level diagram for species **G**, **I**, **J**, and **K** in the transalkylation cycle of the bimolecular isomerization and disproportionation of *m*-xylene over zeolite Y, TNU-9, and ZSM-23.

Table 4. Relative Energies of Species G, I, J, and K of the Bimolecular Isomerization and Disproportionation of *m*-Xylene over Three Different Zeolites

	relative energy (kJ mol^{-1})		
species[a]	zeolite Y	TNU-9	ZSM-23
G	0	0	0
I	−42	−4	153
J	−82	12	135
K	−37	85	184
G′	−7	20	5

[a]The same as those given in Scheme 1.

intermediates in this 1D medium-pore zeolite. Therefore, it is clear that the monomolecular 1,2-methyl shift mechanism is prevailing in the narrower 1D zeolites. In line with our recent experimental work,[15] in this regard, the key to determining the reaction mechanism of *m*-xylene isomerization and disproportionation over medium-pore zeolites may be the availability of large void spaces which can accommodate bulky reaction intermediates.

CONCLUSIONS

In an attempt to theoretically investigate the effects of zeolite pore topology on the isomerization and disproportionation of

dx.doi.org/10.1021/cs500186y | ACS Catal. 2014, 4, 1764−1776

m-xylene over medium-pore zeolites, we have calculated the strain energies of three 3mDPM and six 4mDPM isomers, the main reaction intermediates of this aromatic hydrocarbon conversion, in eight medium-pore zeolites with different framework structures, as well as in the large-pore zeolite Y. The strain energies of these bicyclic aromatic reaction intermediates and the extents of deviation of their central sp^3 carbon angles were found to become higher within zeolites with narrower void spaces. For example, the strain energies of 3mDPM and 4mDPM derivatives are always lower than 40 kJ mol^{-1} in zeolite Y, MCM-22, TNU-9, and NU-87, all of which have 12-ring cavities/channels. When imbedded in ZSM-22 and ZSM-23 with narrow 1D 10-ring channels, all of them are characterized by the strain energies much higher than 40 kJ mol^{-1}. We have also calculated the relative energies of all species associated with the bimolecular isomerization and disproportionation of *m*-xylene over zeolite Y in order to more quantitatively understand the mechanism proposed based on the experimental results. The proton migration from the Brønsted acid sites in zeolite Y to the aromatic ring of a neutral 3mDPM species has the highest energy barrier (76 kJ mol^{-1}) among all the elementary steps after *m*-tolylmethylium cation formation. However, the energy barrier to form 4mDPM species by reaction of the (dimethylphenyl)methylium ion with another *m*-xylene is not higher than 30 kJ mol^{-1} so that it is much lower than that (183 kJ mol^{-1}) to the hydride transfer from the reactant *m*-xylene molecule, a competing step with the formation of tetramethylated benzenium-type carbenium ions. On the other hand, the relative energies of both 3mDPM and 4mDPM species were calculated to become significantly higher when embedded in ZSM-23 with narrow 10-ring channels. This again confirms the importance of the size of zeolitic void spaces in the formation of bulky aromatic reaction intermediates during the bimolecular isomerization and disproportionation of *m*-xylene.

■ ASSOCIATED CONTENT

Supporting Information

Bond angles for the isomers, D_i values, structural depictions using ball-and-stick models, and optimized geometries. This material is available free of charge via the Internet at http://pubs.acs.org.

■ AUTHOR INFORMATION

Corresponding Author

*E-mail: sbhong@postech.ac.kr.

Notes

The authors declare no competing financial interest.

■ ACKNOWLEDGMENTS

This work was supported by the National Creative Research Initiative Program (2012R1A3A2048833) and the BK 21-plus Program through the National Research Foundation of Korea. We thank Dr. A. Zheng, Wuhan Institute of Physics and Mathematics, for helpful discussions.

■ REFERENCES

(1) Tsai, T.-C.; Liu, S.-B.; Wang, I. *Appl. Catal., A* **1999**, *181*, 355−398.
(2) Min, H.-K.; Hong, S. B. *Korean Chem. Eng. Res.* **2013**, *51*, 1−9.
(3) Sulikowski, B. *React. Kinet. Catal. Lett.* **1986**, *31*, 215−219.
(4) Corma, A.; Sastre, E. *J. Catal.* **1991**, *129*, 177−185.
(5) Pérez-Pariente, J.; Sastre, E.; Fornés, V.; Martens, J. A.; Jacobs, P. A.; Corma, A. *Appl. Catal.* **1991**, *69*, 125−137.
(6) Vinek, H.; Lercher, J. A. *J. Mol. Catal. A* **1991**, *64*, 23−39.
(7) Adair, B.; Chen, C.-Y.; Wan, K.-T.; Davis, M. E. *Microporous Mater.* **1996**, *7*, 261−270.
(8) Morin, S.; Gnep, N. S.; Guisnet, M. *J. Catal.* **1996**, *159*, 296−304.
(9) Morin, S.; Ayrault, P.; Gnep, N. S.; Guisnet, M. *Appl. Catal., A* **1998**, *166*, 281−292.
(10) Degnan, T. F., Jr. *J. Catal.* **2003**, *216*, 32−46.
(11) Laforge, S.; Martin, D.; Paillaud, J. L.; Guisnet, M. *J. Catal.* **2003**, *220*, 92−103.
(12) Laforge, S.; Martin, D.; Guisnet, M. *Microporous Mesoporous Mater.* **2004**, *67*, 235−244.
(13) Akpolat, O.; Gündüz, G. *J. Appl. Sci.* **2005**, *5*, 236−248.
(14) Smit, B.; Maesen, T. L. M. *Nature* **2008**, *451*, 671−678.
(15) Min, H.-K.; Cha, S. H.; Hong, S. B. *ACS Catal.* **2012**, *2*, 971−981.
(16) Svelle, S.; Olsbye, U.; Lillerud, K.-P.; Kolboe, S.; Bjørgen, M. *J. Am. Chem. Soc.* **2006**, *128*, 5618−5619.
(17) Xiong, Y.; Rodewald, P. G.; Chang, C. D. *J. Am. Chem. Soc.* **1995**, *117*, 9427−9431.
(18) Min, H.-K.; Chidambaram, V.; Hong, S. B. *J. Phys. Chem. C* **2009**, *114*, 1190−1193.
(19) Min, H.-K.; Hong, S. B. *J. Phys. Chem. C* **2011**, *115*, 16124−16133.
(20) Klein, H.; Kirschhock, C.; Fuess, H. *J. Phys. Chem.* **1994**, *98*, 12345−12360.
(21) Deka, R. C.; Vetrivel, R.; Miyamoto, A. *Top. Catal.* **1999**, *9*, 225−234.
(22) Rozanska, X.; van Santen, R. A.; Hutschka, F.; Hafner, J. *J. Am. Chem. Soc.* **2001**, *123*, 7655−7667.
(23) Rozanska, X.; Saintigny, X.; van Santen, R. A.; Hutschka, F. *J. Catal.* **2001**, *202*, 141−155.
(24) Šponer, J. E.; Šponer, J.; Čejka, J. *J. Mol. Struct.: THEOCHEM* **2001**, *540*, 145−152.
(25) Rozanska, X.; van Santen, R. A.; Hutschka, F. *J. Phys. Chem. B* **2002**, *106*, 4652−4657.
(26) Clark, L. A.; Sierka, M.; Sauer, J. *J. Am. Chem. Soc.* **2003**, *125*, 2136−2141.
(27) Clark, L. A.; Sierka, M.; Sauer, J. *J. Am. Chem. Soc.* **2004**, *126*, 936−947.
(28) Demuth, T.; Raybaud, P.; Lacombe, S.; Toulhoat, H. *J. Catal.* **2004**, *222*, 323−337.
(29) Llopis, F. J.; Sastre, G.; Corma, A. *J. Catal.* **2006**, *242*, 195−206.
(30) Millini, R.; Perego, C. *Top. Catal.* **2009**, *52*, 42−66.
(31) Baerlocher, Ch.; McCusker, L. Database of Zeolite Structures: http://www.iza-structure.org/databases/.
(32) Frisch, M. J.; Trucks, G. W.; Schlegel, H. B.; Scuseria, G. E.; Robb, M. A.; Cheeseman, J. R.; Scalmani, G.; Barone, V.; Mennucci, B.; Petersson, G. A.; Nakatsuji, H.; Caricato, M.; Li, X.; Hratchian, H. P.; Izmaylov, A. F.; Bloino, J.; Zheng, G.; Sonnenberg, J. L.; Hada, M.; Ehara, M.; Toyota, K.; Fukuda, R.; Hasegawa, J.; Ishida, M.; Nakajima, T.; Honda, Y.; Kitao, O.; Nakai, H.; Vreven, T.; Montgomery, J. A.; Peralta, J. E.; Ogliaro, F.; Bearpark, M.; Heyd, J. J.; Brothers, E.; Kudin, K. N.; Staroverov, V. N.; Kobayashi, R.; Normand, J.; Raghavachari, K.; Rendell, A.; Burant, J. C.; Iyengar, S. S.; Tomasi, J.; Cossi, M.; Rega, N.; Millam, J. M.; Klene, M.; Knox, J. E.; Cross, J. B.; Bakken, V.; Adamo, C.; Jaramillo, J.; Gomperts, R.; Stratmann, R. E.; Yazyev, O.; Austin, A. J.; Cammi, R.; Pomelli, C.; Ochterski, J. W.; Martin, R. L.; Morokuma, K.; Zakrzewski, V. G.; Voth, G. A.; Salvador, P.; Dannenberg, J. J.; Dapprich, S.; Daniels, A. D.; Farkas, O.; Foresman, J. B.; Ortiz, J. V.; Cioslowski, J.; Fox, D. J. *Gaussian 09*, revision C.01; Gaussian, Inc.: Wallingford, CT, 2010.
(33) Chai, J.; Head-Gordon, M. *Phys. Chem. Chem. Phys.* **2008**, *10*, 6615−6620.
(34) Yi, X.; Byun, Y.; Chu, Y.; Zheng, A.; Hong, S. B.; Deng, F. *J. Phys. Chem. C* **2013**, *117*, 23626−23637.
(35) Van der Mynsbrugge, J.; Hemelsoet, K.; Vandichel, M.; Waroquier, M.; Van Speybroeck, V. *J. Phys. Chem. C* **2012**, *116*, 5499−5508.
(36) Solans-Monfort, X.; Sodupe, M.; Branchadell, V.; Sauer, J.; Orlando, R.; Ugliengo, P. *J. Phys. Chem. B* **2005**, *109*, 3539−3545.
(37) Sillar, K.; Burk, P. *J. Phys. Chem. B* **2004**, *108*, 9893−9899.
(38) Jansang, B.; Nanok, T.; Limtrakul, J. *J. Phys. Chem. B* **2006**, *110*, 12626−12631.

(39) Boekfa, B.; Pantu, P.; Limtrakul, J. *J. Mol. Struct.* **2008**, *889*, 81−88.
(40) Boekfa, B.; Choomwattana, S.; Khongpracha, P.; Limtrakul, J. *Langmuir* **2009**, *25*, 12990−12999.
(41) Kumsapaya, C.; Bobuatong, K.; Khongpracha, P.; Tantirungrotechai, Y.; Limtrakul, J. *J. Phys. Chem. C* **2009**, *113*, 16128−16137.
(42) Boekfa, B.; Pantu, P.; Probst, M.; Limtrakul, J. *J. Phys. Chem. C* **2010**, *114*, 15061−15067.
(43) Fang, H.; Zheng, A.; Xu, J.; Li, S.; Chu, Y.; Chen, L.; Deng, F. *J. Phys. Chem. C* **2011**, *115*, 7429−7439.
(44) Wattanakit, C.; Nokbin, S.; Boekfa, B.; Pantu, P.; Limtrakul, J. *J. Phys. Chem. C* **2012**, *116*, 5654−5663.
(45) Pauling, L. *The Nature of the Chemical Bond*; Cornell University Press: Ithaca, NY, 1945; pp 111−116.
(46) Hong, S. B.; Min, H.-K.; Shin, C.-H.; Cox, P. A.; Warrender, S. J.; Wright, P. A. *J. Am. Chem. Soc.* **2007**, *129*, 10870−10885.
(47) Willems, T. F.; Rycroft, C. H.; Kazi, M.; Meza, J. C.; Haranczyk, M. *Microporous Mesoporous Mater.* **2012**, *149*, 134−141.